AGU PUBLICATIONS

Water Resources Research

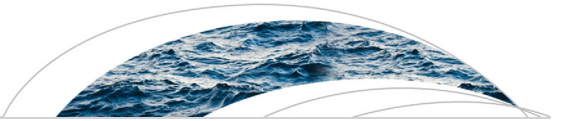

RESEARCH ARTICLE

10.1002/2017WR021083

Key Points:
- A differential imaging-based porous plate method is devised to visualize brine distribution during capillary drainage with micro-CT
- The sequence of capillary-controlled pore filling in a laminated sandstone is determined with a pore-scale interpretation of displacement
- The capillary pressure measurements agree with porous plate experiments on a larger core but with much shorter experimental time

Supporting Information:
- Supporting Information S1

Correspondence to:
Q. Lin,
q.lin11@imperial.ac.uk

Citation:
Lin, Q., B. Bijeljic, H. Rieke, and M. J. Blunt (2017), Visualization and quantification of capillary drainage in the pore space of laminated sandstone by a porous plate method using differential imaging X-ray microtomography, *Water Resour. Res.*, *53*, 7457–7468, doi:10.1002/2017WR021083.

Received 10 MAY 2017
Accepted 2 AUG 2017
Accepted article online 7 AUG 2017
Published online 29 AUG 2017

Visualization and quantification of capillary drainage in the pore space of laminated sandstone by a porous plate method using differential imaging X-ray microtomography

Qingyang Lin[1], Branko Bijeljic[1], Holger Rieke[2], and Martin J. Blunt[1]

[1]Department of Earth Science and Engineering, Imperial College London, London, United Kingdom, [2]DEA, Deutsche Erdoel AG, Hamburg, Germany

Abstract The experimental determination of capillary pressure drainage curves at the pore scale is of vital importance for the mapping of reservoir fluid distribution. To fully characterize capillary drainage in a complex pore space, we design a differential imaging-based porous plate (DIPP) method using X-ray microtomography. For an exemplar mm-scale laminated sandstone microcore with a porous plate, we quantify the displacement from resolvable macropores and subresolution micropores. Nitrogen (N_2) was injected as the nonwetting phase at a constant pressure while the porous plate prevented its escape. The measured porosity and capillary pressure at the imaged saturations agree well with helium measurements and experiments on larger core samples, while providing a pore-scale explanation of the fluid distribution. We observed that the majority of the brine was displaced by N_2 in macropores at low capillary pressures, followed by a further brine displacement in micropores when capillary pressure increases. Furthermore, we were able to discern that brine predominantly remained within the subresolution micropores, such as regions of fine lamination. The capillary pressure curve for pressures ranging from 0 to 1151 kPa is provided from the image analysis compares well with the conventional porous plate method for a cm-scale core but was conducted over a period of 10 days rather than up to few months with the conventional porous plate method. Overall, we demonstrate the capability of our method to provide quantitative information on two-phase saturation in heterogeneous core samples for a wide range of capillary pressures even at scales smaller than the micro-CT resolution.

1. Introduction

The characterization of multiphase flow properties and behavior within complex geological porous media are important in many applications including hydrocarbon recovery, carbon storage, and contaminant transport [*Gelhar et al.*, 1992; *Fredd and Fogler*, 1998; *Gaus et al.*, 2008; *Blunt et al.*, 2013]. To achieve this, the experimental determination of representative capillary pressure curves as a function of saturation is required, since capillary pressure is a key parameter for reservoir characterization [*Kalam et al.*, 2006; *Blunt*, 2017], including the initial reservoir fluid distribution and subsequent flow properties under production. To describe and fully explain the physics of displacement processes, pore-scale characterization is of vital importance. This is especially true for complex pore structures for which flow through microporosity plays an important role. Despite progress made on the modeling side for single phase flow and transport [*Bijeljic et al.*, 2011; *Gjetvaj et al.*, 2015; *Soulaine et al.*, 2016] and multiphase flow [*Ramstad et al.*, 2012; *Kallel et al.*, 2016; *Norouzi Apourvari and Arns*, 2016], there has not been an experimental attempt at the pore scale to characterize multiphase flow within microporosity. In our study, we will use laminated sandstone as an exemplar complex rock structure to demonstrate how our new differential imaging method can be used to quantify the role of microporosity on the macroscopic manifestation of multiphase displacement.

The most frequently used techniques to obtain capillary pressure curves at the core scale (∼cm-scale) are porous plate (PP), the mercury intrusion capillary pressure (MICP) technique, and the centrifuge method [*Hassler and Brunner*, 1945; *Darling*, 2005; *Kalam et al.*, 2006; *Pini et al.*, 2012]. These techniques are routinely applied in the oil industry as a part of Special Core Analysis (SCAL) to obtain reservoir rock properties [*Darling*, 2005; *Masalmeh and Jing*, 2008]. Of these, the porous plate technique is usually considered to be accurate and reliable. It can normally be combined with other measurements (e.g., measurements for resistivity

index); it ensures a relatively homogeneous saturation profile; and it allows further analysis with the same core [*Kalam et al*., 2006]. The main disadvantage of the porous plate method is that it is time consuming, taking up to a few months to obtain the full capillary pressure curve [*Kennedy*, 2015]. On the other hand, MICP measurements are fast and provide access to very small pores. However, this technique is destructive which prevents the use of the same sample for further measurements. Furthermore, since mercury is used to occupy the pore space at vacuum conditions, it does not record the irreducible wetting phase saturation at high capillary pressure, which is observed in experiments where water or brine is displaced. The centrifuge technique [*Hassler and Brunner*, 1945] is an alternative method in which water invades a saturated core plug with a nonwetting fluid by high speed centrifuging. The disadvantage of the method is that it is impossible to obtain drainage, spontaneous imbibition, forced water injection, and secondary drainage curves, as well as the inability to combine with other petrophysical measurements, e.g., resistivity index [*Kalam et al*., 2006]. Furthermore, all these techniques do not measure the spatial distribution of the fluids in the pore space, which is at the heart of understanding and interpreting multiphase flow behavior, in particular for complex pore structures containing microporosity. To address this issue, we propose a novel method for measurement of both multiphase fluid which makes the use of both X-ray tomography and a conventional porous plate technique.

A porous ceramic plate is hydrophilic with a uniform pore size distribution and provides a certain breakthrough pressure but is permeable only to the wetting phase thus preventing breakthrough of the nonwetting (displacing) phase. At the same time, the porous plate ensures that the pressure of the wetting phase remains constant throughout the core at displacement equilibrium conditions. Although the traditional porous plate method can provide reliable capillary pressure curves, it is difficult to fully understand the origin of multiphase flow behavior without in situ visualization. Combining this technique with imaging is important and necessary to better understand the process and provide reliable information on spatially resolved fluid distributions which can further be used in pore-scale models.

In recent years, micro-CT has been widely used in geologically related studies [*Ketcham and Carlson*, 2001; *Cnudde and Boone*, 2013; *Lin et al*., 2016a; *Al-Khulaifi et al*., 2017; *Reyes et al*., 2017; *Saif et al*., 2017], especially for visualizing multiphase flow, measuring contact angle, and obtaining capillary pressure from curvature measurements in the pore space [*Arns et al*., 2005; *Armstrong et al*., 2012; *Iglauer et al*., 2012; *Blunt et al*., 2013; *Andrew et al*., 2014a,b; *Schlüter et al*., 2014]. To visualize and understand flow properties as a function of rock geometry and topology, accurate imaging methods are essential. One of the main barriers is to characterize subresolution pores, the issue of particular interest in heterogeneous subsurface rock with a wide distribution in pore size. *Lin et al*. [2016b] developed an experimental method based on differential imaging to visualize and quantify subresolution pores in carbonate rock using high salinity brine. However, identification of multiple phases at resolutions higher than micron scale and estimating fluid saturation still pose significant challenges.

Our main goal is to fully describe the displacement physics during capillary drainage in complex pore spaces by providing spatially resolved fluid distributions which include microporosity—to achieve this, we design a new methodology which combines the porous plate method with X-ray microtomography (micro-CT). Our scientific contributions include (a) quantitative experimental characterization of multiphase displacement in microporous regions of an exemplar rock whose pore space is not fully resolvable by X-ray tomography, (b) the observation of the sequence of filling during capillary-controlled displacement, and (c) provision of quantitative datasets for a new generation of pore-scale models which address multiphase flow within microporosity. We therefore introduce a new differential imaging-based porous plate method (which we call the DIPP method) that uses a high salinity brine to visualize the fluid distribution in macropores and microporosity during capillary drainage using micro-CT. We use nitrogen (N_2) as the nonwetting phase and potassium iodide (KI) doped brine as the wetting phase. We demonstrate our method on a microcore (4.86 mm in diameter) from a laminated sandstone core plug for a range of capillary pressures from 0 to 1151 kPa. We measure the average saturation and the spatial distribution of the wetting phase and analyze the drainage behavior. The capillary pressure curve is then compared with the measurements obtained using both MICP and the conventional porous plate technique at the cm-scale (35 mm in diameter) to assess the capability and accuracy of our method. The contribution to displacement from macropores and microporosity are quantified to characterize the displacement physics during capillary drainage.

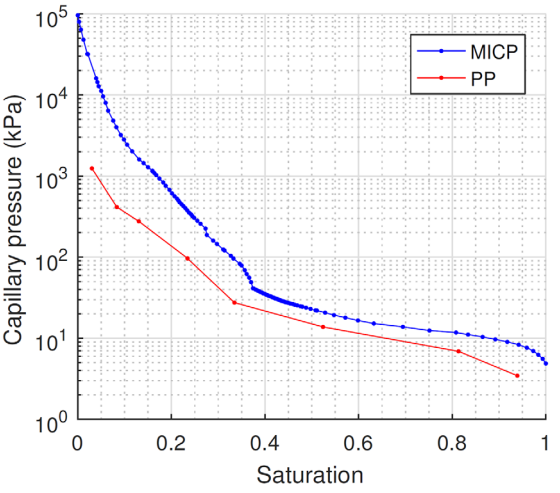

Figure 1. The capillary pressure curves using MICP and conventional porous plate (PP) methods as a function of wetting phase saturation (water for the PP method and vacuum for MICP). The capillary pressure curve from MICP is converted to an equivalent curve under air/brine system from its original air/mercury system using equation (1).

2. Materials and Methods

2.1. Materials

The rock sample we used is a Rotliegend sandstone with fine laminations from a producing natural gas field. The micro-CT samples were drilled into cylindrical cores (4.86 mm in diameter and 14.0 mm in length) from the original core (35 mm in diameter). The total porosity of the sample using MICP and helium (He) measurements were 0.163 and 0.164, respectively. Based on the MICP measurements (supporting information Figure S2), there are approximately 20% of the pores within the sample below the 5 μm voxel size which we used for micro-CT imaging. The details of MICP can be found in supporting information section S2.

2.2. Capillary Pressure Measurements From MICP and Conventional Porous Plate Technique

The capillary pressure curves at the core scale include both MICP and porous plate methods (conducted by Panterra Geoconsultants, Netherlands). The capillary pressure measurement from the conventional porous plate method used the original core plug. The brine saturated core was placed with a saturated porous disc in series. After applying confining pressure, air was injected at different pressures to displace brine. At different pressure stages, once the system had reached capillary equilibrium, the sample is weighed to determine the loss of liquid and calculate the average saturation. The air pressure was increased until no further brine displacement was observed. Desaturation continues until no more weight loss is observed, at which time the sample is at irreducible water saturation. In a core of this size, capillary equilibrium at each pressure stage typically took several days to be achieved, leading to a total experimental time of up to few months.

Figure 1 shows the capillary pressure curves from both the MICP and conventional porous plate methods. The comparison of different capillary curves using different methods, including the micro-CT imaging technique introduced in this study, is discussed in section 3.3. To compare the MICP results (air/mercury system) and the results from the porous plate method (air/brine system), the capillary pressures from MICP have been multiplied by a factor given by *Leverett* [1941], *Darling* [2005], and *Blunt* [2017]:

$$\frac{P_{c(\text{gas/brine})}}{P_{c(\text{gas/mercury})}} = \frac{(\gamma\cos\theta)_{(\text{air/brine})}}{(\gamma\cos\theta)_{(\text{air/mercury})}} = \frac{72\ \cos 0^\circ}{480\ \cos 40^\circ} = 0.20 \quad (1)$$

where P_c is the capillary pressure, γ is the interfacial tension: 72 mN/m for the air/brine system and 480 mN/m for the air/mercury system [*Darling*, 2005], and θ is the contact angle.

Figure 1 shows that there is a poor agreement between the two measurement methods. For a given capillary pressure, the predicted water saturation, for the same rock, differ by around 0.1, which could lead to very poor estimates of gas or oil in place in a hydrocarbon field. The discrepancy is unlikely to be due to an irreducible water saturation in the porous plate method, since the MICP results predict higher saturations. The core is heterogeneous with fine-scale laminations. The differences between the methods may be caused by this heterogeneity and the volumes of the samples used, but there is no way to determine which is the more representative measurement without knowing the distribution of fluid within the core.

2.3. Experimental Methodology for DIPP

The experimental apparatus for the differential imaging-based porous plate method (DIPP method) is shown in Figure 2. The core was then attached to a hydrophilic porous ceramic plate with a certain breakthrough pressure, and then placed into a fluoro-polymer elastomer (Viton) sleeve, which was attached to metal fittings (end piece) connecting the core to the pore fluid flow lines.

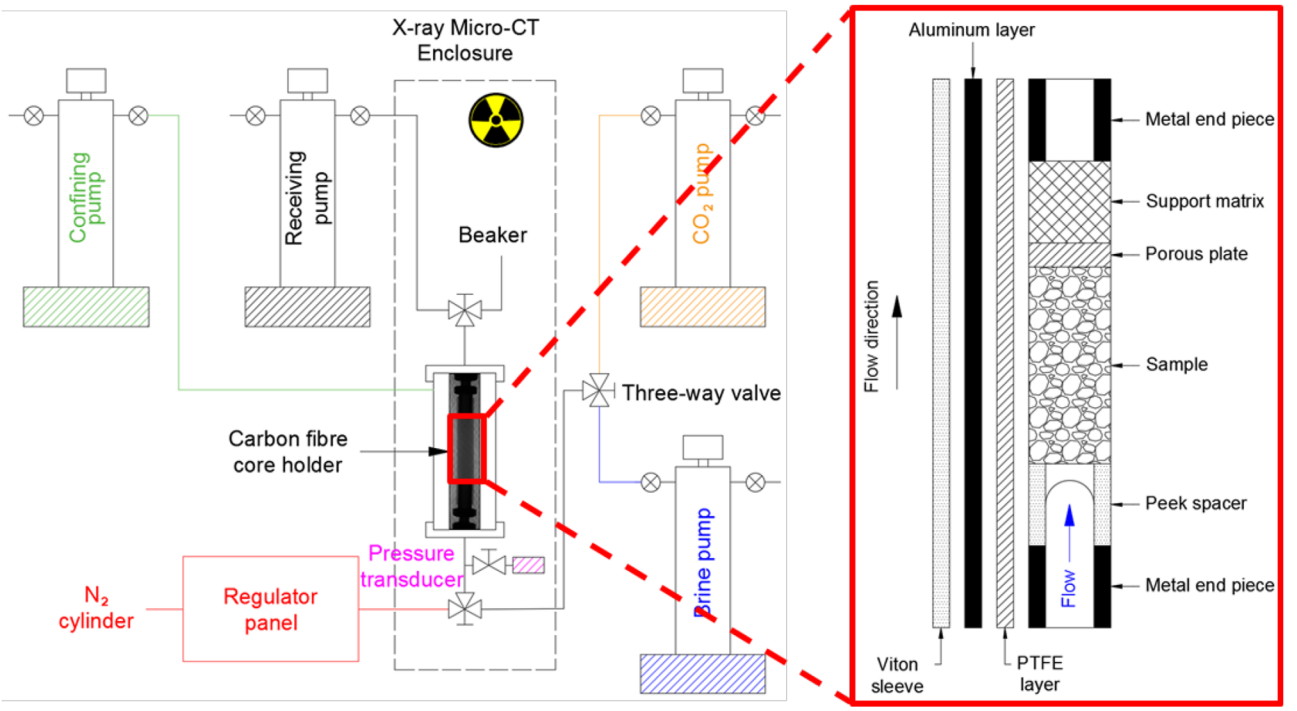

Figure 2. Experimental apparatus. (a) The pump system to control flow. (b) Detail of the core assembly.

The brine solution was made from deionized water with a prescribed amount of potassium iodide (KI). KI was used as an ionic salt as it has a high atomic weight causing a high X-ray attenuation coefficient, allowing it to be used as a contrast agent. In this study, to visualize the brine in subresolution pores, 30 wt % KI was selected [*Lin et al*., 2016b].

The maximum capillary pressure in the reservoir from which the laminated sandstone originated is approximately 1000 kPa. To capture brine distributions for a wide range of capillary pressures, two porous plates with different breakthrough pressures were used: one for the low pressure range (up to 103 kPa) and the other for the high pressure range (up to 1151 kPa).

The experiment was conducted using the following procedure:

1. A confining pressure of 3000 kPa was applied and maintained within the cell to compress the Viton sleeve around the core sample to avoid any fluid bypass.
2. A dry (air) scan was taken at room temperature.
3. After 100% brine saturation was achieved, a brine saturated scan was taken.
4. At ambient pressure, the production line was switched from the receiving pump to the beaker. This was done to provide a visual inspection when injecting N_2 as the nonwetting phase at a certain capillary pressure.
5. The N_2 was then injected at a constant pressure controlled by the regulator. The capillary pressure for the drainage pressure was controlled by maintaining the pressure difference between the inlet pressure and outlet pressure (ambient pressure). At a certain capillary pressure, the nonwetting phase (N_2) displaced the wetting phase (KI doped brine) and was prevented from escaping the system by the porous plate (500 kPa breakthrough pressure).
6. When there was no more brine displaced by N_2, which was indicated by no further droplets coming out from the production side into the beaker, a scan of the core partially saturated with brine was taken.
7. Steps 5 and 6 were then repeated with the injection pressure gradually increased.
8. When the injection pressure reached 103 kPa, the whole system was depressurized and the core sample was cleaned and dried.

As described above, we used two porous plates with 500 and 1500 kPa breakthrough pressures to cover the wide range of capillary pressures (supporting information Table S1). After the maximum capillary

pressure was reached with the first porous plate, it was replaced with the second plate and Steps 1–8 were repeated until the highest capillary pressure was attained. The whole experiment was performed over a period of 10 days. The capillary pressure steps for the drainage process are 7, 14, 21, 38, 71, 103, 206, 483, and 1151 kPa (also shown in supporting information Table S2).

3. Results and Discussion

We first introduce the differential imaging-based method which provides spatially resolved maps of the pore space filled with two fluids including subresolution porosity (sections 3.1 and 3.2). This is then followed by an analysis of the capillary pressure curve in terms of macroporosity and subresolution porosity in section 3.3. Here two-stage capillary drainage is identified, characterizing the physics of multiphase displacement in a laminated sandstone with a complex pore structure and demonstrating the capability of our technique to use rich observations from micro-CT imaging to interpret the macroscopic manifestation of displacement behavior.

3.1. Characterization of Pore Structure

The differential image with 30 wt % KI concentration allows enhanced phase contrast [*Lin et al.*, 2016b]. The image analysis procedure is as follows: the dry scan of the laminated sandstone core was used as the reference scan. The 30 wt % KI saturated scan and the scan after drainage at different capillary pressures were registered to the reference scan to have the same orientation using normalized mutual information, and resampled using the Lanczos algorithm [*Burger and Burge*, 2010]. The voxel size for all the scans was 5.0 μm. The differential image between the scan with KI in the pore space and the dry scan is obtained from:

$$\mathrm{CT\ (differential)} = \mathrm{CT\ (KI)} - \mathrm{CT\ (Dry)} + \mathrm{CT0} \tag{2}$$

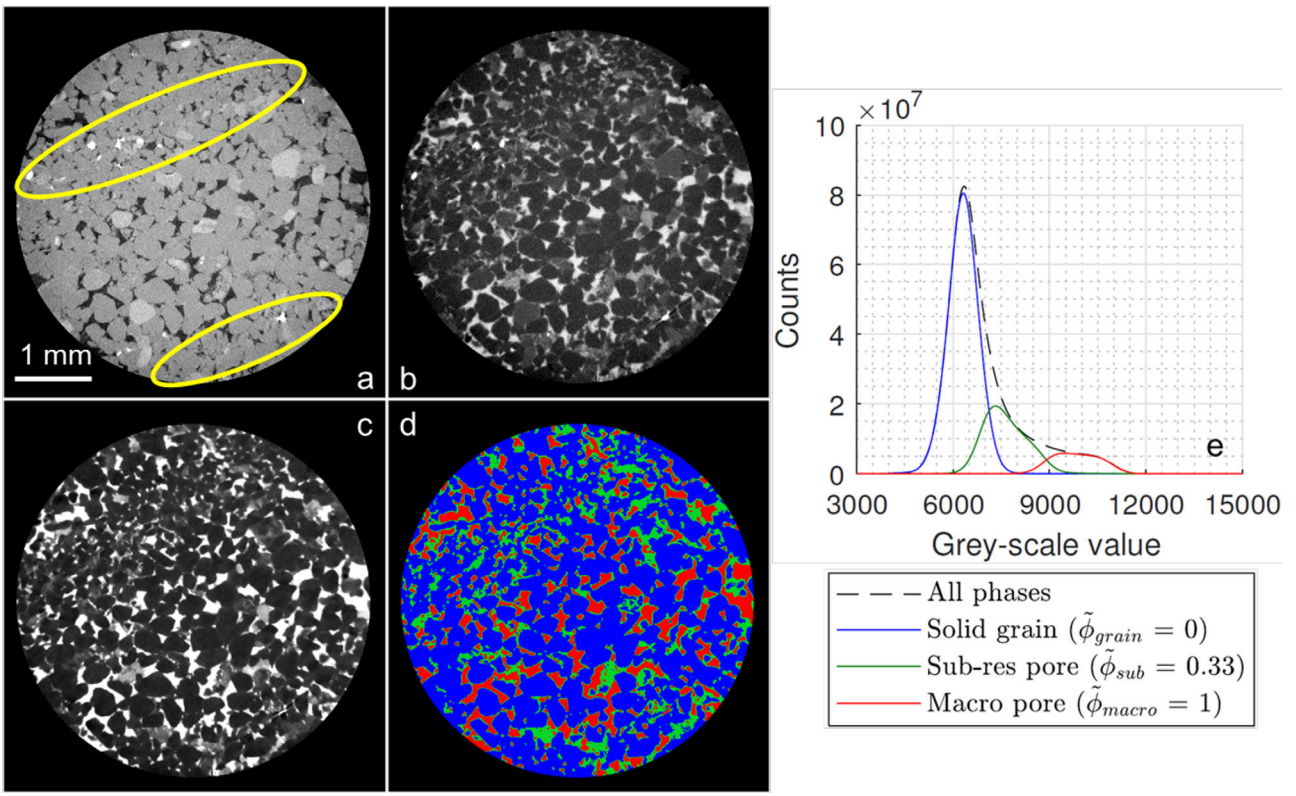

Figure 3. Three-phase segmentation including subresolution pores for Rotliegend sandstone: (a) an example slice from the original dry scan. The laminations are indicated. (b) The same slice showing the core saturated with 30 wt % KI. (c) The difference image between the KI saturated scan and the dry scan after applying a nonlocal means filter. (d) Three-phase segmentation showing grain (blue), subresolution pores (green), and macropores (red). (e) The histograms for the three phases in the KI saturated scan are plotted based on the segmented label images using global thresholding method. The average porosity within the subresolution region can be quantified and is 0.33 in this example.

where CT is the CT number of each voxel and CT0 is some large positive constant (65,535 in this example) to avoid negative values. Before extracting information from image analysis, a nonlocal means edge preserving filter [*Buades et al*., 2008] was applied to these differential images to reduce the image noise.

Using global thresholding, three-phase segmentation (supporting information Figure S3) can be performed based on the differential image [*Lin et al*., 2016b]. Accordingly, the filtered differential image was processed with global thresholding to identify solid grain phase, subresolution phase, and macropore phase. The resultant three-phase segmented label images and the histograms for the three phases for the imaged sample are shown in Figure 3.

The average porosity within the subresolution pores ($\tilde{\phi}_{sub}$) can now also be quantified using:

$$\tilde{\phi}_{sub}=\left(\frac{\tilde{\phi}_{macro}-\tilde{\phi}_{grain}}{CT_{macro}-CT_{grain}}\right)\left(CT_{sub}-CT_{grain}\right)=\frac{CT_{sub}-CT_{grain}}{CT_{macro}-CT_{grain}} \tag{3}$$

where CT_{grain} is the grey-scale value where the peak values located in the histogram are denoted as for solid grain phase, CT_{sub} is the representative grey-scale value for the subresolution pore phase, and CT_{macro} is the representative grey-scale value for the macropore phase. In the KI saturated images, the porosity for the grain phase ($\tilde{\phi}_{grain}$) is assumed to be 0 and the average porosity values for the macropore phase ($\tilde{\phi}_{macro}$) is assumed to be 1. The total porosity (ϕ_{total}), including subresolution pores, of the field of view within the entire sample from image processing using the equation below, is 0.166:

$$\phi_{total}=\tilde{\phi}_{grain}V_{grain}+\tilde{\phi}_{sub}V_{sub}+\tilde{\phi}_{macro}V_{macro} \tag{4}$$

where $\tilde{\phi}_{grain}$ is 0, $\tilde{\phi}_{macro}$ is 1, $\tilde{\phi}_{sub}$ is 0.33, and V_{grain}, V_{sub}, and V_{macro} are the total volume fraction for each phase which can be obtained from the segmented label images in Figure 3d. This result compares well with a helium porosity measurement on the entire sample with a total porosity of 0.170 $\pm$ 0.004.

3.2. Brine Distribution During Capillary Drainage Using DIPP

Figure 4 shows the same slice displaying the brine distribution at different exemplar capillary pressures. Due to the high concentration of the contrast fluid (30 wt % KI), the brine phase appears brighter in all the grey-scale images. It can be observed that after capillary drainage at low capillary pressures (0–38 kPa), the majority of the brine (wetting phase) initially residing in the macropores has been displaced by N_2 (nonwetting phase). The remaining brine can be seen from the brighter regions with higher grey-scale values compared to the same regions in the preceding scans. Most of these regions are in the laminations and within some grains with subresolution porosity. At higher capillary pressures (>38 kPa), it is difficult to visualize the brine phase in the macropore space as most of the brine remained in the subresolution pores. Therefore, image processing based on differential imaging needs to be applied to visualize and quantify the brine distribution and its saturation values at different capillary pressures—we accomplish this by applying an image normalization method described below.

3.2.1. Image Normalization

The average brine saturation value within the subresolution pores is the key parameter to quantify the total brine distribution at different capillary pressures. At a low capillary pressure where brine was present in the macropores, the average brine saturation can be easily quantified using the same histogram-based method used for quantifying subresolution porosity after generating the differential image (shown in Figure 3e). However, when the brine only remained in subresolution pores at high capillary pressures, the representative value for the brine phase (such as the peak value in the histogram for the brine phase at low capillary pressures) could not be readily obtained, and the histogram-based method cannot be performed to calculate the average brine saturation. Therefore, before generating differential images, it is necessary to normalize all the images to have the same grey-scale range for the rock phase and brine phase.

This image normalization is conducted by normalizing all the images using the representative grey-scale values for the overall rock matrix phase and a selected dense mineral within the rock matrix phase (mineral grain rendered in blue on the dry scan, shown in Figure 5). The criterion for selecting the dense mineral for calibration is that the representative grey-scale value for this mineral should be similar to the representative value for the brine phase in the macropores. This is presented in supporting information Figure S4 which shows the histogram plots for the brine phase and the dense mineral in the brine saturated scan. During

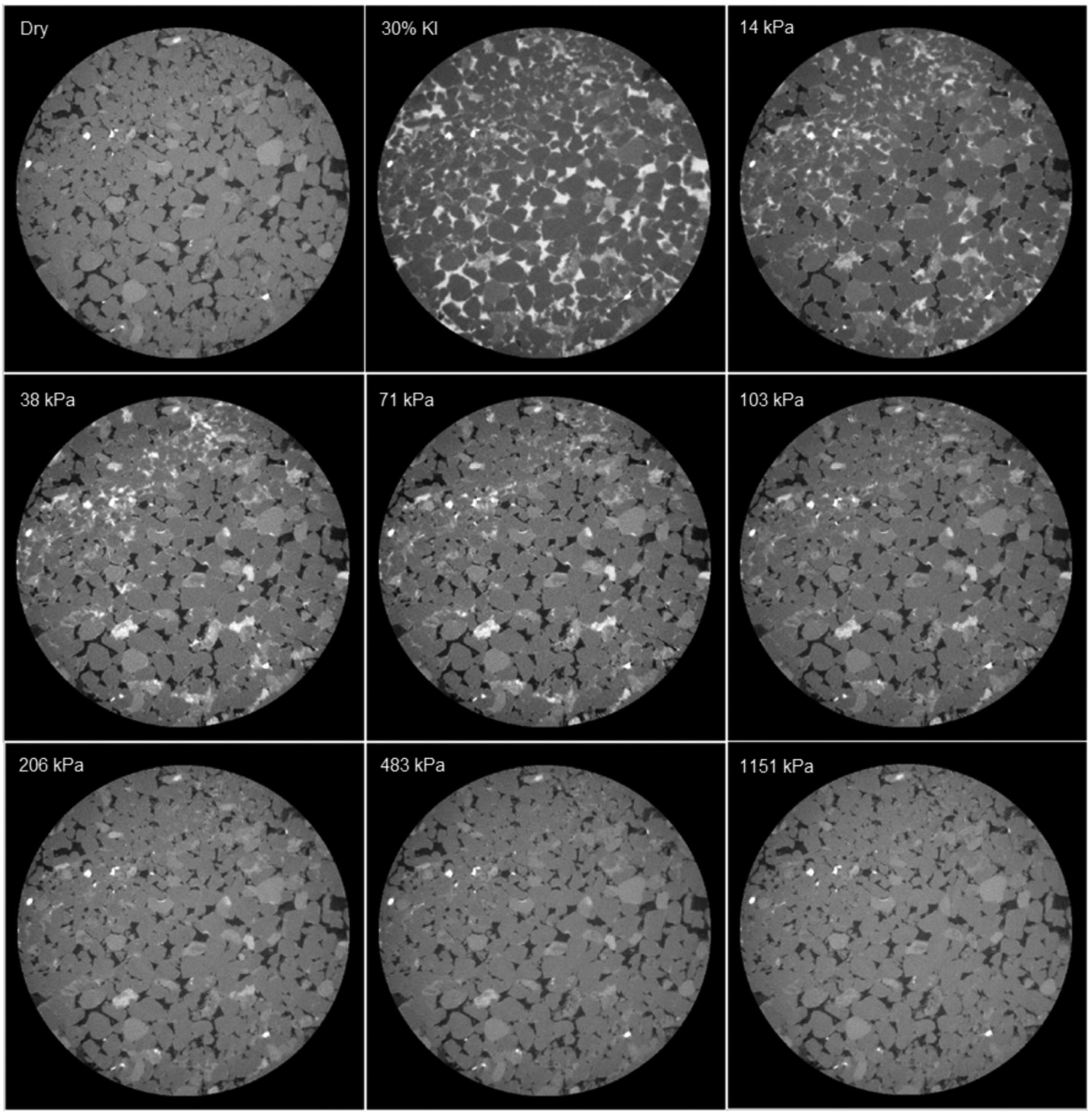

Figure 4. The same slice in dry scan, KI saturated scan and scans after drainage at different exemplar capillary pressure values. The bright phase in the images is the brine.

the image normalization, the histogram for the rock phase and the selected mineral grain can be plotted. The example from the dry scan shown in Figure 5 is used for demonstration. The representative grey-scale value for the rock phase (CT_0) and the representative grey-scale value for the mineral grain (CT_m) for each scan can be obtained. The histogram of the whole image was then normalized by ensuring CT_0 and CT_m matching the corresponding reference values, Ref_0 and Ref_m, using:

$$Hist_n = \frac{Hist(Ref_m - Ref_0)}{CT_m - CT_0} + \frac{CT_m Ref_0 - CT_0 Ref_m}{CT_m - CT_0} \quad (5)$$

where $Hist$ is the histogram of the image before normalization, $Hist_n$ is the histogram of the image after normalization, CT_0 is the representative grey-scale value for the rock phase in the image before normalization, CT_m is the representative grey-scale value for the mineral phase in the image before normalization, Ref_{rock} is the reference value for a representative grey-scale value of the rock phase after normalization (8000 in

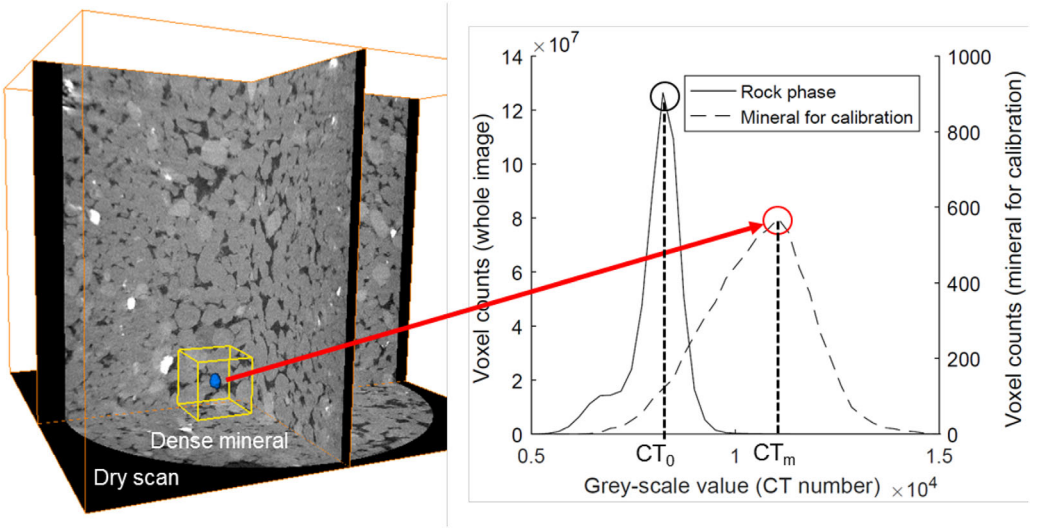

Figure 5. (a) Visualization of the dry scan with the selected dense mineral for calibration, rendered in blue. (b) Histogram showing the representative grey-scale values for rock phase and for the dense mineral phase, used for calibration. The representative grey-scale value for the rock phase was used as the value representing solid phase with 0% brine.

this study), and Ref_m is the reference value for the representative grey-scale value of the mineral phase after normalization (11,000 in this study). The representative grey-scale value for the rock phase, CT_0, was used as solid phase and the brine saturation is assumed as 0.

The main purpose of the image normalization step is to ensure that the representative grey-scale values for the rock phase and brine phase are the same. After image normalization, the representative value for the brine phase (CT_1) in the KI saturated scan was calculated again (supporting information Figure S4) and this value, which is 10,537, was assumed to be the representative value for all the normalized images. The brine saturation for the brine in the macropores, $\tilde{\phi}_{brine\_1}$, is assumed to be 1.

3.2.2. Average Brine Saturation at Different Capillary Pressures

After image normalization, the differential image between the image taken after each drainage step at a given capillary pressure and the dry scan can be generated, followed by applying a nonlocal means edge preserving filter [*Buades et al.*, 2008]. An example slice from the differential image after drainage at 7 kPa (after filtering) is shown in Figure 6. Three-phase segmentation using a global thresholding [*Lin et al.*, 2016b] was performed

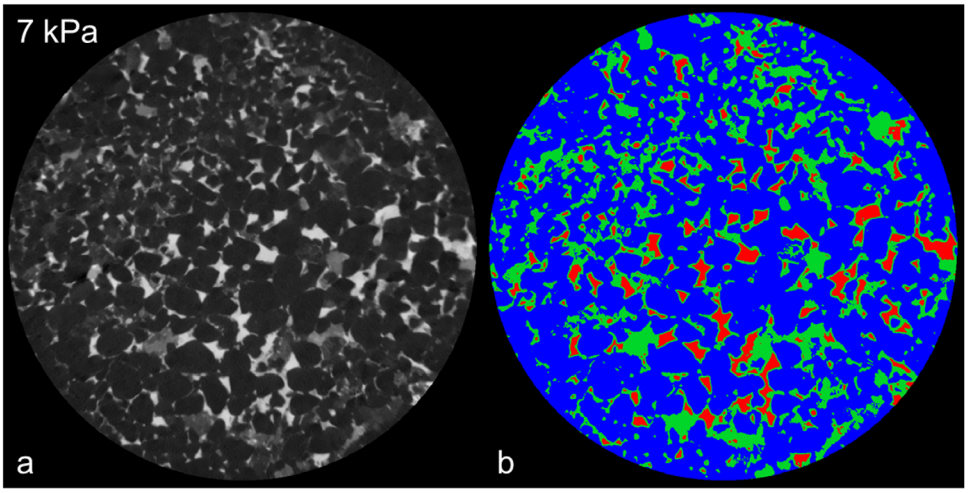

Figure 6. (a) An example slice from the differential image after drainage at 7 kPa (after filtering). (b) Three-phase segmentation using a global thresholding, showing the regions with 0% brine (blue), regions with subresolution pores filled with brine at a certain brine saturation (green) and the macropores filled with 100% brine (red). The regions with 0% brine contain both solid grains the macropores filled with N_2 (brine in the pores has been displaced).

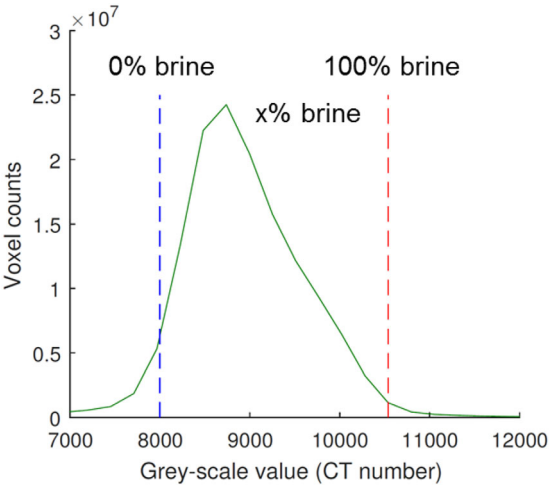

Figure 7. The histogram plot of the grey-scale values for the voxels in the subresolution pores filled with brine. The grey-scale value (CT_X) represents the brine remaining in the subresolution pores and can be used to calculate the average brine saturation ($\tilde{\phi}_{brine\_X}$) within the subresolution pores.

showing the regions with 0% brine (blue), regions with subresolution pores filled with brine at a certain brine saturation (green) and the macropores filled with 100% brine (red). It needs to be noted that the regions with 0% brine contains both solid grains the macropores filled with N_2 (brine in the pores has been displaced).

After image normalization, the grey-scale values which represent 0% brine (CT_0) and 100% brine (CT_1) have already been determined. To obtain the total brine saturation, the average brine saturation within the subresolution pores needs to be determined. This can be conducted by extracting the voxels with brine remained in the subresolution pores (green) in Figure 6b and plotting the histogram of the grey-scale values for these voxels from the image after each drainage process (Figure 6a) at each capillary pressure. The histogram is shown in Figure 7. The average brine saturation within the subresolution pores, $\tilde{\phi}_{brine\_X}$, can be calculated as

$$\tilde{\phi}_{brine\_X}=\left(\frac{\tilde{\phi}_{brine\_1}-\tilde{\phi}_{brine\_0}}{CT_1-CT_0}\right)(CT_X-CT_0)=\frac{CT_X-CT_0}{CT_1-CT_0} \tag{6}$$

where CT_X is the grey-scale value represents the subresolution pores filled with brine.

3.3. Analysis of Capillary Pressure Behavior From DIPP Method

The total brine saturation after each drainage process (S_w) can be described as the sum of contributions from macropores (f_{brine_1}), and within subresolution pores (f_{brine_X}):

$$S_w=\frac{f_{brine\_X}+f_{brine\_1}}{\phi_{pore}} \tag{7}$$

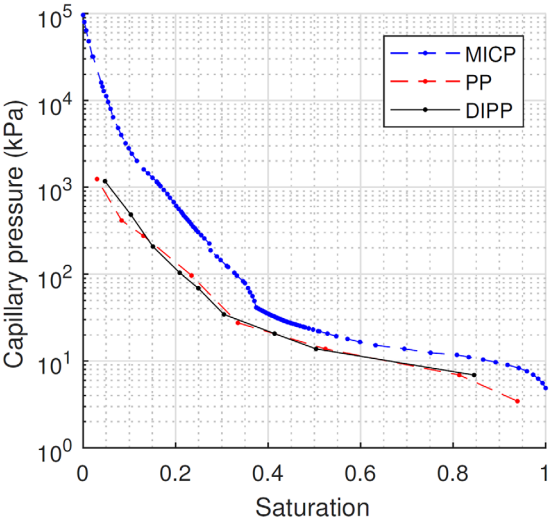

Figure 8. Capillary pressure against wetting phase saturation. The results obtained by our differential imaging-based method (DIPP) compare well with the results of the conventional porous plate method (PP) but are significantly different from that measured by mercury injection (MICP).

where ϕ_{pore} is the total porosity of the sample, which is 0.166.

$$f_{brine\_1}=\tilde{\phi}_{brine\_1}V_1 \tag{8}$$

$$f_{brine\_X}=\tilde{\phi}_{brine\_X}V_X \tag{9}$$

where the value of $\tilde{\phi}_{brine\_X}$ for the capillary pressure of 7 kPa case is 0.294 (from Figure 7), and the value of $\tilde{\phi}_{brine\_1}$ is 1. V_1 and V_X are the total volume fraction for each phase which can be obtained from the segmented label images in Figure 6b, which are in this case 0.259 and 0.676, respectively. The total brine saturation can be therefore calculated as 0.845 from equation (7). The values for $\tilde{\phi}_{brine\_X}$ after each capillary drainage step at different capillary pressures are shown later in Figure 10. A slight decrease in the average brine saturation within subresolution regions ($\tilde{\phi}_{brine\_X}$) from 0 to 38 kPa can be observed, followed by a more significant decrease when capillary pressure increases.

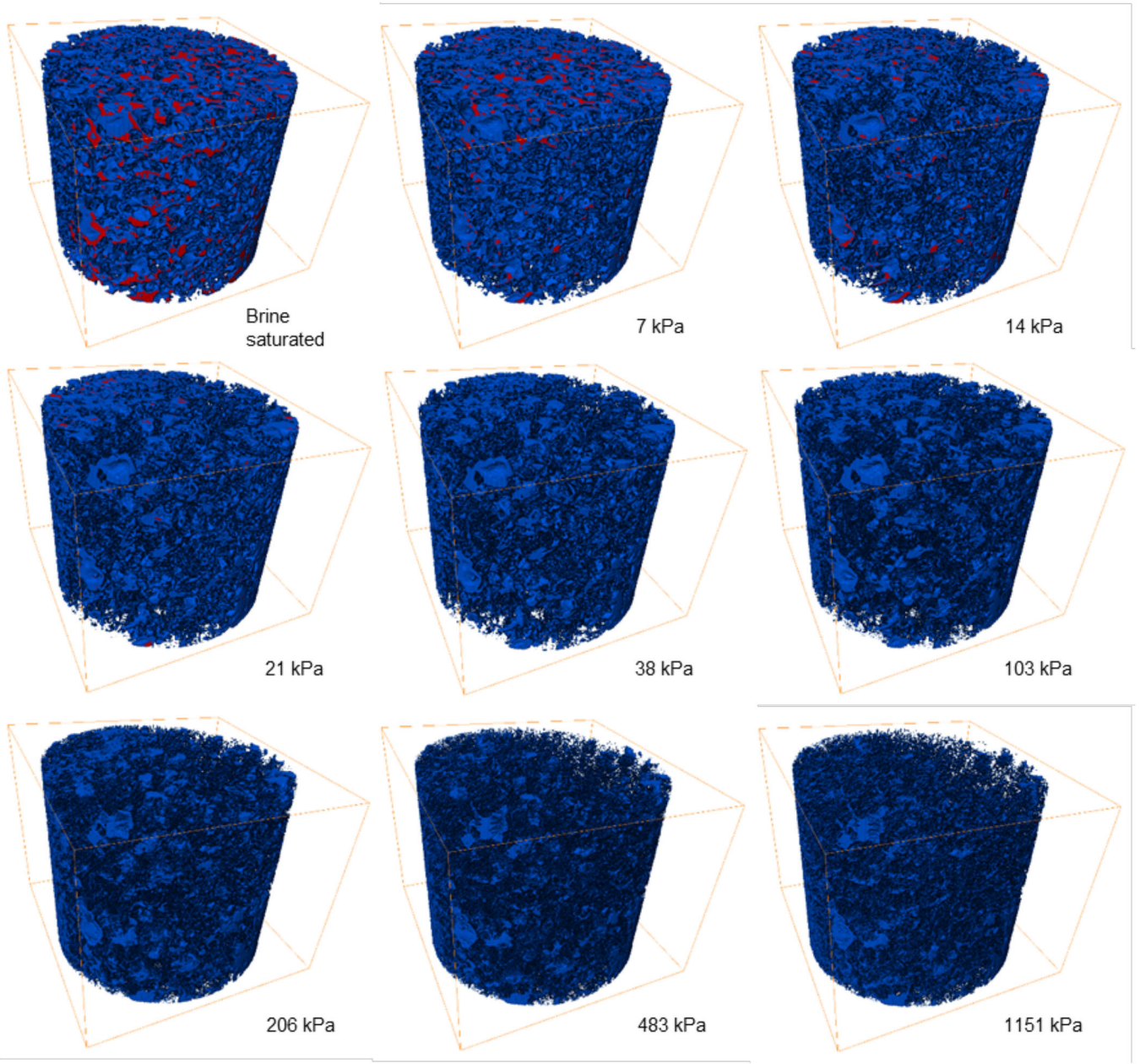

Figure 9. 3-D visualizations of the brine distribution within the pore space after capillary drainage at different capillary pressures. Red shows the brine within macropores while blue is the brine within subresolution pores.

After applying this method to analyze all the images taken during drainage, the capillary pressure as a function of brine saturation for a range of pressures from 0 to 1151 kPa can be calculated. Figure 8 shows the comparison of capillary pressure obtained by our new differential imaging-based method (DIPP) and those obtained using both MICP and the conventional porous plate method.

The measurements obtained by the DIPP method show a good agreement with the measurements performed using the conventional porous plate method (PP) on the original core. The capillary pressure curve from the MICP method is different from both curves obtained by the porous plate methods. This indicates that the MICP method does not provide a representative capillary curve for this sample with fine laminations. Apart from being a destructive method, another main disadvantage for the MICP method is that is performed on small dry samples using mercury as the nonwetting phase and air as the wetting phase which only serve as a proxy for reservoir fluids [*Newsham et al.*, 2004]. Therefore, conversion of the capillary

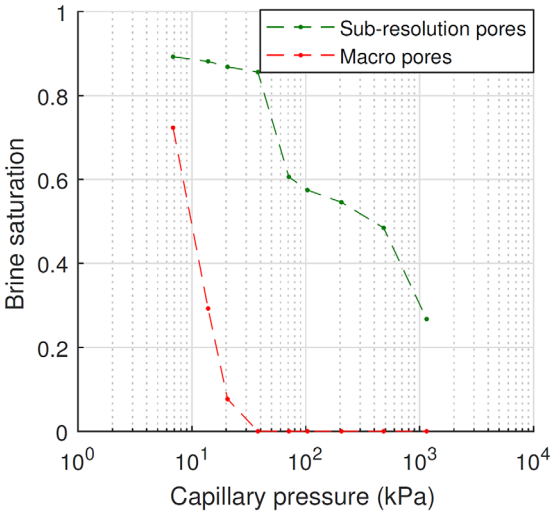

Figure 10. Saturation of brine remaining in both macropores and subresolution pores after each capillary drainage step at different capillary pressures.

pressure between air/mercury system and gas/brine system is required (see equation (1)) and this comes with some uncertainty. It is also appears that in the MICP experiment, the mercury was unable to access some of the fine laminations.

Apart from much faster experimental time (10 days comparing to up to few months for the conventional porous plate method), another main advantage of the DIPP approach is that we can see the fluid distribution at the pore scale, to interpret the results, to understand the displacement process, and to gain some confidence in their validity: Figure 9 shows a 3-D visualization of the brine distribution within the pore space after capillary drainage at different capillary pressures. In red is the brine within macropores while blue is the brine within subresolution pores. Two-stage brine displacement can be directly observed and quantified. When the capillary pressure increases from 0 to 38 kPa, the brine phase remained within subresolution pores with little displacement, whereas almost all the brine in the macropores was displaced by N_2, which can be seen as the rapid reduction of the volume in red. When the capillary pressure increases from 38 to 1151 kPa, the brine within subresolution pores was gradually displaced, until it reached an apparent irreducible saturation of only around 5%.

The amount of brine left within both macro and subresolution pores can be quantitatively analyzed, as shown in Figure 10, indicating a two-stage displacement. At low capillary pressures, the displacement almost exclusively occurred in the macropores. In the capillary pressure range from 0 to 38 kPa, almost all the brine within macropores was displaced, whereas only a small amount of brine displacement occurred within subresolution pores. Further displacement within subresolution pores occurred at capillary pressures higher than 38 kPa.

4. Conclusions

We have provided first experimental insights into the role of multiphase flow within microporosity during a capillary drainage in a complex pore space of an exemplar laminated sandstone. We have demonstrated the capability of a high salinity brine (30 wt % KI) differential imaging method, DIPP, to image and visualize capillary drainage displacement sequence using a porous plate technique. We verify the porosity characterization by comparing image-measured porosity with a helium porosity measurement.

We observe a two-stage capillary drainage displacement: at low capillary pressures (up to 38 kPa), the brine is displaced only from macropores but remains in lamination layers and grains within subresolution pores; this is followed by brine displacement within subresolution pores at higher capillary pressures. The capillary pressure curve for a range of pressures from 0 to 1151 kPa is provided from the image analysis, and shows good agreement with conventional porous plate measurements on a larger core sample. However, the capillary pressure curve is different from that measured using mercury injection (MICP) which indicates that, in some cases, MICP may not be the most reliable method, since it does not use representative fluids.

Assuming that a representative sample is studied, the experiments using DIPP are much faster: a flooding sequence can be completed in 10 days, as opposed to up to several months for the conventional porous plate method (PP). Crucially, we have developed an experimental capability to visualize and quantify multiphase fluid distribution in both macropores and microporosity over a wide range of capillary pressures, including the maximum capillary pressure encountered in the reservoir. This allows for the physics of the displacement behavior to be understood at the pore scale. The acquired images with fluid distributions in

the pore space can be potentially used as input into pore-scale models for predictions of properties outside the range studied experimentally.

Acknowledgments
We gratefully acknowledge funding from DEA Deutsche Erdoel AG. The data acquired are available from the corresponding author upon request.

References

Al-Khulaifi, Y., Q. Lin, M. J. Blunt, and B. Bijeljic (2017), Reaction rates in chemically heterogeneous rock: Coupled impact of structure and flow properties studied by X-ray microtomography, *Environ. Sci. Technol.*, *51*(7), 4108–4116, doi:10.1021/acs.est.6b06224.

Andrew, M., B. Bijeljic, and M. J. Blunt (2014a), Pore-by-pore capillary pressure measurements using X-ray microtomography at reservoir conditions: Curvature, snap-off, and remobilization of residual CO_2, *Water Resour. Res.*, *50*, 8760–8774, doi:10.1002/2014WR015970.

Andrew, M., B. Bijeljic, and M. J. Blunt (2014b), Pore-scale contact angle measurements at reservoir conditions using X-ray microtomography, *Adv. Water Resour.*, *68*, 24–31, doi:10.1016/j.advwatres.2014.02.014.

Armstrong, R. T., M. L. Porter, and D. Wildenschild (2012), Linking pore-scale interfacial curvature to column-scale capillary pressure, *Adv. Water Resour.*, *46*, 55–62, doi:10.1016/j.advwatres.2012.05.009.

Arns, C. H., et al. (2005), Pore scale characterization of carbonates using X-ray microtomography, *SPE J.*, *10*(4), 475–484, doi:10.2118/90368-PA.

Bijeljic, B., S. Rubin, H. Scher, and B. Berkowitz (2011), Non-Fickian transport in porous media with bimodal structural heterogeneity, *J. Contam. Hydrol.*, *120*, 213–221, doi:10.1016/j.jconhyd.2010.05.007.

Blunt, M. J. (2017), *Multiphase Flow in Permeable Media: A Pore-Scale Perspective*, Cambridge Univ. Press, Cambridge, U. K.

Blunt, M. J., B. Bijeljic, H. Dong, O. Gharbi, S. Iglauer, P. Mostaghimi, A. Paluszny, and C. Pentland (2013), Pore-scale imaging and modelling, *Adv. Water Resour.*, *51*, 197–216, doi:10.1016/j.advwatres.2012.03.003.

Buades, A., B. Coll, and J.-M. Morel (2008), Nonlocal image and movie denoising, *Int. J. Comput. Vis.*, *76*(2), 123–139, doi:10.1007/s11263-007-0052-1.

Burger, W., and M. J. Burge (2010), *Principles of Digital Image Processing*: Core Algorithms, Undergraduate Topics in Computer Science, Springer, London.

Cnudde, V., and M. N. Boone (2013), High-resolution X-ray computed tomography in geosciences: A review of the current technology and applications, *Earth Sci. Rev.*, *123*, 1–17, doi:10.1016/j.earscirev.2013.04.003.

Darling, T. (2005), *Well Logging and Formation Evaluation*, Elsevier, Hoboken, N. J.

Fredd, C. N., and H. S. Fogler (1998), Influence of transport and reaction on wormhole formation in porous media, *AIChE J.*, *44*(9), 1933–1949, doi:10.1002/aic.690440902.

Gaus, I., P. Audigane, L. André, J. Lions, N. Jacquemet, P. Durst, I. Czernichowski-Lauriol, and M. Azaroual (2008), Geochemical and solute transport modelling for CO_2 storage, what to expect from it?, *Int. J. Greenhouse Gas Control*, *2*(4), 605–625, doi:10.1016/j.ijggc.2008.02.011.

Gelhar, L. W., C. Welty, and K. R. Rehfeldt (1992), A critical review of data on field-scale dispersion in aquifers, *Water Resour. Res.*, *28*(7), 1955–1974, doi:10.1029/92WR00607.

Gjetvaj, F., A. Russian, P. Gouze, and M. Dentz (2015), Dual control of flow field heterogeneity and immobile porosity on non-Fickian transport in Berea sandstone, *Water Resour. Res.*, *51*, 8273–8293, doi:10.1002/2015WR017645.

Hassler, G. L., and E. Brunner (1945), Measurement of capillary pressures in small core samples, *Trans. Am. Inst. Min. Metall. Pet. Eng.*, *160*(1), 114–123.

Iglauer, S., M. A. Fernø, P. Shearing, and M. J. Blunt (2012), Comparison of residual oil cluster size distribution, morphology and saturation in oil-wet and water-wet sandstone, *J. Colloid Interface Sci.*, *375*(1), 187–192, doi:10.1016/j.jcis.2012.02.025.

Kalam, M. Z., K. Al Hammadi, O. B. Wilson, M. Dernaika, and H. Samosir (2006), Importance of porous plate measurements on carbonates at pseudo reservoir conditions, in SCA2006-28, presented at the 2006 SCA International Symposium, Trondheim, Norway.

Kallel, W., M. I. J. van Dijke, K. S. Sorbie, R. Wood, Z. Jiang, and S. Harland (2016), Modelling the effect of wettability distributions on oil recovery from microporous carbonate reservoirs, *Adv. Water Resour.*, *95*, 317–328, doi:10.1016/j.advwatres.2015.05.025.

Kennedy, M. (2015), *Practical Petrophysics*, Elsevier, Hoboken, N. J.

Ketcham, R. A., and W. D. Carlson (2001), Acquisition, optimization and interpretation of X-ray computed tomographic imagery: Applications to the geosciences, *Comput. Geosci.*, *27*, 381–400, doi:10.1016/S0098-3004(00)00116-3.

Leverett, M. C. (1941), Capillary behavior in porous solids, *Trans. Am. Inst. Min. Metall. Pet. Eng.*, *142*(1), 152–169, doi:10.2118/941152-G.

Lin, Q., S. J. Neethling, L. Courtois, K. J. Dobson, and P. D. Lee (2016a), Multi-scale quantification of leaching performance using X-ray tomography, *Hydrometallurgy*, *164*, 265–277, doi:10.1016/j.hydromet.2016.06.020.

Lin, Q., Y. Al-Khulaifi, M. J. Blunt, and B. Bijeljic (2016b), Quantification of sub-resolution porosity in carbonate rocks by applying high-salinity contrast brine using X-ray microtomography differential imaging, *Adv. Water Resour.*, *96*, 306–322, doi:10.1016/j.advwatres.2016.08.002.

Masalmeh, S. K., and X. D. Jing (2008), The importance of special core analysis in modelling remaining oil saturation in carbonate fields, in Proceedings of the International Symposium of the Society of Core Analysis.

Newsham, K. E., J. A. Rushing, P. M. Lasswell, J. C. Cox, and T. A. Blasingame (2004), A comparative study of laboratory techniques for measuring capillary pressures in tight gas sands, paper presented at the SPE Annual Technical Conference and Exhibition, Soc. of Pet. Eng, Houston, Tex.

Norouzi Apourvari, S., and C. H. Arns (2016), Image-based relative permeability upscaling from the pore scale, *Adv. Water Resour.*, *95*, 161–175, doi:10.1016/j.advwatres.2015.11.005.

Pini, R., S. C. M. Krevor, and S. M. Benson (2012), Capillary pressure and heterogeneity for the CO_2/water system in sandstone rocks at reservoir conditions, *Adv. Water Resour.*, *38*, 48–59, doi:10.1016/j.advwatres.2011.12.007.

Ramstad, T., N. Idowu, C. Nardi, and P.-E. Øren (2012), Relative permeability calculations from two-phase flow simulations directly on digital images of porous rocks, *Transp. Porous Media*, *94*(2), 487–504, doi:10.1007/s11242-011-9877-8.

Reyes, F., Q. Lin, O. Udoudo, C. Dodds, P. D. Lee, and S. J. Neethling (2017), Calibrated X-ray micro-tomography for mineral ore quantification, *Miner. Eng.*, *110*, 122–130, doi:10.1016/j.mineng.2017.04.015.

Saif, T., Q. Lin, B. Bijeljic, and M. J. Blunt (2017), Microstructural imaging and characterization of oil shale before and after pyrolysis, *Fuel*, *197*, 562–574, doi:10.1016/j.fuel.2017.02.030.

Schlüter, S., A. Sheppard, K. Brown, and D. Wildenschild (2014), Image processing of multiphase images obtained via X-ray microtomography: A review, *Water Resour. Res.*, *50*, 3615–3639, doi:10.1002/2014WR015256.

Soulaine, C., F. Gjetvaj, C. Garing, S. Roman, A. Russian, P. Gouze, and H. A. Tchelepi (2016), The impact of sub-resolution porosity of X-ray microtomography images on the permeability, *Transp. Porous Media*, *113*(1), 227–243, doi:10.1007/s11242-016-0690-2.